Sol–gel synthesis of NiFe$_2$O$_4$ with PVA matrices and their catalytic activities for one-step hydroxylation of benzene into phenol

Ibraheem Othman Ali

Abstract Nickel ferrite (NiFe$_2$O$_4$) was synthesized using citric acid (CA) as a chelating agent and varying amounts of polyvinyl alcohol (PVA) as powder binder via a combustion process. The influence of PVA/NiFe$_2$O$_4$ blend composition on the phase, crystal structure, and morphology has been investigated by X-ray diffraction (XRD), scanning electron microscopy, and Fourier transform infrared spectroscopy, respectively. The probable assignments of the thermal degradation products of PVA/NiFe$_2$O$_4$ were studied by complementary thermogravimetric analysis and differential thermal analysis. The PVA/NiFe$_2$O$_4$ crystals preferentially oriented along the (311) plane as revealed by XRD, owing to diffusion of α-Fe$_2$O$_3$ particles into the lattice matrix where the rate of diffusion increased significantly with the PVA concentration increase from 0.1 to 0.3 mol%. A vibrational doublet at 1,644 and 1,609 cm^{-1} for the ≡Fe–O–COOH complex was emitted in the spectra of PVA-impregnated NiFe$_2$O$_4$ to assure the attachment of Fe(III) to the chelating agents CA/PVA. Thermal kinetic consideration based on Coats–Redfern and Horowitz–Metzger equations at subsequent decomposition steps of CA/PVA/NiFe$_2$O$_4$ illustrated that the values of activation free energy ΔG* increase significantly, indicating the non-spontaneous behavior. The one-step direct hydroxylation of benzene toward phenol has been extensively investigated using hydrogen peroxide as an oxidant.

Keywords Inorganic compounds · Chemical synthesis · Sol–gel growth · Crystal structure · Thermogravimetric analysis (TG)

I. O. Ali (✉)
Department of Chemistry, Faculty of Science, Al-Azhar University, Nasr City 11884, Cairo, Egypt
e-mail: Ibraheem_othman2002@yahoo.com

List of symbols

PVA	Polyvinyl alcohol
CA	Citric acid
XRD	X-ray diffraction analysis
FT-IR	Fourier transform infrared
E	Activation energy (kJ mol^{-1})
ΔG^*	Activation Gibbs free energy change (kJ mol^{-1})
ΔH^*	Activation enthalpy change (kJ mol^{-1})
ΔS^*	Entropy change (kJ mol^{-1})
A	Arrhenius factor (S^{-1})
T	Kelvin temperature (K)
CR	Coats–Redfern
HM	Horowitz–Metzger
W_f	Mass loss at the completion of the reaction
W	Mass loss
TG	Thermogravimetric analysis
DTA	Differential thermal analysis
SEM	Scanning electron micrographs
R	Universal gas constant
k	Boltzmann constants
h	Planck constants

Introduction

Crystalline ferrites having general formula MFe$_2$O$_4$ (M = divalent metal ion, e.g., Ni, Co, Cu, etc.) are one of the most attracting materials due to their various applications such as transformer core, antenna rod, recording head, loading coil, memory and microwave devices [1]. Practical applications of ferrites include household, electronics, and computers. Apart from their technological importance in the electronic and magnetic industries, ferrites exhibit properties such as various redox states, electrochemical

stability, pseudocapacitive behavior, etc., and nowadays, they can be used in supercapacitors and in Li batteries [2, 3]. It is established that various binary and ternary spinel ferrites are effective catalysts for a number of industrial processes such as oxidative dehydrogenation of hydrocarbons [4], decomposition of alcohols and hydrogen peroxide [5], treatment of automobile-exhaust gases [6], oxidation of various compounds such as CO [7], phenol hydroxylation [8], alkylation reaction [9], etc.

Nickel ferrite ($NiFe_2O_4$) with an inverse spinel structure shows ferrimagnetism, which originates from magnetic moment of anti-parallel spins between Fe^{3+} ions at tetrahedral sites and Ni^{2+} ions at octahedral sites [10]. As more and more attentions have been devoted to the nano-sized magnetic materials for their unique and amazing properties compared to their bulk counterparts, the scientific interests were focused on nano-sized nickel ferrite [11]. $NiFe_2O_4$ is also employed in a wide variety of catalytic and photo-catalytic processes such as total oxidation of propane [12] and toluene [13], photocatalytic water remediation [14], decomposition of N_2O [15], oxidative dehydrogenation of 1-butene to 1,3-butadiene [16], and methane combustion [17]. Moreover, this catalyst showed high degradation efficiency of di-*n*-butyl phthalate in ozonation catalytic system with convenient separation [18]. Nanoferrites are usually prepared by various physical methods [19, 20], as well as chemical methods like mechanical milling, inert gas condensation, hydrothermal reaction, oxidative precipitation, and sol–gel synthesis techniques [21, 22]. The sol–gel auto-combustion route, as a unique combination of the combustion and the chemical gelation process, is preferred in general because of its main advantages of inexpensive precursors, short preparation time, modest heating, and relatively simple manipulations [23–25].

Synthesis procedures of spinel ferrite nanoparticles were intensively studied in recent years. Large-scale applications of ferrites with nanoparticles and tailoring of specific properties have prompted the development of several widely used chemical methods [26] like sol–gel [27], host template [28], co-precipitation [29], and hydrothermal treatment [30]. Addition of cationic surfactants with hydrophilic head and hydrophobic tail into the solution results in the formation of reverse micelles [31]. Placing the aqueous ions inside these micelles can affect the controlling of the nucleation and growth of the particles. Due to the existence of surfactant, the surface tension of solution is also reduced, which lowers the energy of the formation of the new phase [31].

In the present work, a new synthesis method of $NiFe_2O_4$ was carried out by adding different amounts of polyvinyl alcohol (PVA) to citric acid (CA) via employing the sol–gel auto-combustion technique, which resulted in lowering the ignition temperature of formation of the pure crystalline

$NiFe_2O_4$ phase. The synthesized catalysts were investigated by Fourier transform infrared (FT-IR) spectroscopy, Thermogravimetric and differential thermal analyses (TG/DTA), X-ray diffraction (XRD), and scanning electron micrograph (SEM) measurements. The catalytic hydroxylation of benzene to phenol in the presence of hydrogen peroxide was chosen as a test reaction and the effect of reaction parameters was investigated.

Experimental

Materials

The used chemical reagents are ferric chloride (Merck), nickel chloride (Merck), ammonia solution, CA, PVA (Fluka) of molecular mass (125,000), benzene, hydrogen peroxide, 4-aminoantipyrine, and potassium ferrocyanate (Fluka).

Synthesis of nickel ferrite ($NiFe_2O_4$)

$NiFe_2O_4$ was prepared by the sol–gel auto-combustion method. 8.5 mol of iron chloride and 3.6 mol nickel chloride powders in a molar ratio of Fe/Ni = 2.63 were mixed together with 8.5 mol of CA, wherein CA helps the homogenous distribution of the metal ions throughout the solution by forming a complex with Fe(III). After adding this solution into 200 mL of deionized water, different amounts of PVA (0.1–0.3 mol%) were added, followed by carefully dipping little drops of ammonia solution to the solution to attain the pH 7. The mixed solution was heated at 353 K for 3 h with continuous stirring to allow a sol–gel reaction to occur through condensation reaction between the metal ions and the PVA to yield a composite network in colloidal state known as sol. The resultant sol was obtained and then dried in an oven at 393 K for 8 h. The dried samples were heated in an oven air for 6 h at 673, 873, and 1173 K, respectively. The samples were referred as PVA-free $NiFe_2O_4$ for PVA-free sample and $0.1PVA/NiFe_2O_4$, $0.2PVA/NiFe_2O_4$, and $0.3PVA/NiFe_2O_4$ where the onset of abbreviates indicate mol% of the loaded PVA.

Physicochemical characterization

XRD data of the samples were measured at room temperature using a Philips diffractometer (type PW 3710). The patterns were run with Ni-filtered copper radiation ($\lambda = 1.5404$ Å) at 30 kV and 10 mA with a scanning speed of $2\theta = 2.5°$ min^{-1}. The mean particle size (D) was calculated using the Debye–Scherrer Eq. (1) [32], in which K is a constant equal to 0.9, λ is the wavelength of the Cu Kα radiation, β is the half peak width of the diffraction peak in radiant, and theta is the Bragg scattering angle.

$$D = K\lambda\beta\cos\theta. \tag{1}$$

The FT-IR spectra were recorded on a Perkin Elmer Spectrum (RXI FT-IR) system, single-beam spectrometer with a resolution of 2 cm^{-1}. The samples were ground with KBr (1:100) as a tablet and mounted to the sample holder in the cavity of the spectrometer. The measurements were recorded at room temperature in the region 4,000–400 cm^{-1}.

Morphology and size of the prepared materials were determined using SEMs for products obtained on a JEOL scanning microscope model JSM-T 330A at an accelerating voltage of 30 kV.

TG/DTA were carried out using Shimadzu-50 thermal analyzer units. The sensitivity of TG and DTA measurements was 0.01 mg and 25 µv, respectively. In each run about 10 mg of uncalcined sample was heated from 303 to 1,273 K at a heating rate of 10 K min^{-1} under a stream of flowing nitrogen at a rate of 30 mL min^{-1}.

Thermal kinetic analysis

The thermal data under investigation were analyzed according to Kissinger equation [33]:

$$\beta\frac{d\alpha}{dt} = Ae^{-E_a/RT}f(\alpha), \tag{2}$$

where α is the fraction reacted (alternatively called conversion degree), T is the absolute temperature, β is the heating rate ($\beta = dT/dt$, where t is the time), A is the pre-exponential factor, E_a is the activation energy, R is the gas constant, and $f(\alpha)$ is the differential form of the reaction model, i.e., a function of α which well fits the experimental data.

The kinetic analysis was performed by means of software kinetic program [34], which includes the majority of reaction models, ranging from 1st to nth order, nucleation-growth model, as well as the activation energy distribution models, and uses a non-linear regression method to determine the parameters of Eq. (2) to fit the experimental data. To check the presumed invariance of E_a on α, the software kinetic program performs the isoconversional "model-free" analysis by means of expanded Horowitz–Metzger (HM) and modified Coats–Redfern (CR) methods [35]. Multi-heating rate application of the CR equation may be expressed by the equation:

$$\log\left[\frac{\log\{f|(W_f - W)\}}{T^2}\right] - \log\left[\frac{AR}{\theta E^*}\left(\frac{1 - 2RT}{E^*}\right)\right]$$
$$- \frac{E^*}{2.303RT}, \tag{3}$$

where W_f is the mass loss at the completion of the reaction, W is the mass loss at Kelvin temperature T, R is the gas constant, E^* is the activation energy in kJ mol^{-1}, θ is the heating rate, and $(1 - 2RT/E^*) \approx 1$. A plot of the left-hand side of Eq. (3) against $1/T$ gives a slope from which E^* was calculated and A was determined from the intercept.

Alternatively, we applied the HM equation [36, 37] to the thermal data for the materials under study which may be written in the form:

$$\log\left(\frac{W_\infty}{W_r}\right) = \frac{\theta E^*}{2.302RT_s^2} - \log 2.303, \tag{4}$$

where T_s is the DTG peak temperature and $\theta = T - T_s$. A plot of log [logW_∞/W_r] versus θ will give a straight line with a slope from which E^* can be calculated. The pre-exponential factor A was calculated from the following equation:

$$C = \left(\frac{\theta E^*}{RT_s^2}\right)\exp\left(\frac{E^*}{RT_s}\right). \tag{5}$$

The activation entropy (ΔS^*), activation enthalpy (ΔH^*), and the activation free energy (ΔG^*) were calculated using the following equations [38]:

$$\Delta S^* = 2.303\left[\log\left(\frac{Ah}{kT}\right)\right], \tag{6}$$

$$\Delta H^* = E^* - nRT, \tag{7}$$

$$\Delta G^* = \Delta H^* - T\Delta S^*, \tag{8}$$

where k and h are the Boltzmann and Planck constants, respectively. The calculated values of E^*, A, ΔS^*, ΔH^*, and ΔG^* for the different decomposition steps are given in Table 2.

Catalytic tests

Liquid-phase hydroxylation of benzene to phenol with hydrogen peroxide over the prepared catalysts was conducted in a 250 mL batch glass reactor equipped with a condenser under atmospheric pressure. The catalyst was dried at 383 K in an oven to remove water before weighing into the reactor. 20 mL additional water, apart from that obtained by the H$_2$O$_2$ solution, was normally used, unless stated otherwise, for better dispersion of the catalyst. Magnetic stirring bar and additional water were added before placing the reactor into the oil bath and connecting with the condenser. After heating up this system to reaction temperature, liquid benzene was injected, thereby avoiding excess benzene evaporation during the heating up process. H$_2$O$_2$ was slowly added dropwise to the reactor with the help of an appropriate syringe during the first 10 min of the reaction. In a typical reaction, 0.011 mol of H$_2$O$_2$ and x mol of benzene ($x = 0.011$, 0.022, 0.033, 0.044, or 0.055 mol) were used. The reaction was carried out for 3 h at 343 K under vigorous stirring. After the reaction has stopped, the concentration of phenol being obtained solely
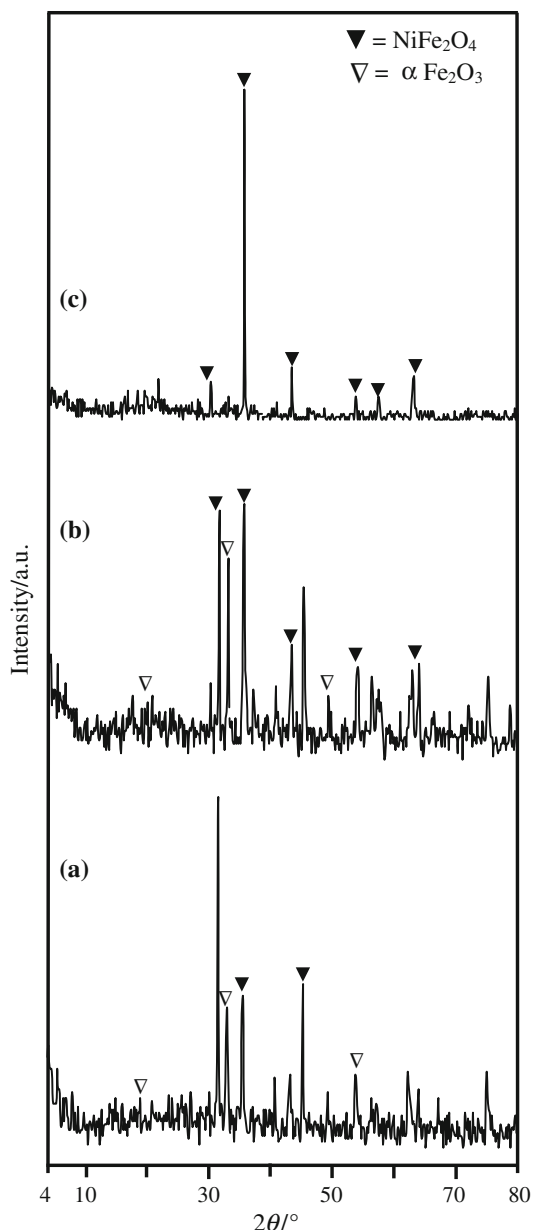
Fig. 1 XRD patterns of CA/PVA/NiFe$_2$O$_4$ (molar ratio PVA:CA = 5:1) calcined at (*a*) 673 K, (*b*) 873 K, and (*c*) 1,173 K

was determined at $\lambda_{max} = 510$ nm using spectrophotometery by the 4-aminoantipyrine method [39, 40].

Results and discussion

XRD analysis

The XRD examination of the thermally treated 0.2PVA/NiFe$_2$O$_4$ at 673 and 873 K showed strong diffractions at *d*-spacings 3.68, 2.71, and 1.69 Å related to α-Fe$_2$O$_3$, the others at 2.95 and 4.82 Å are due to NiFe$_2$O$_4$ (Fig. 1).
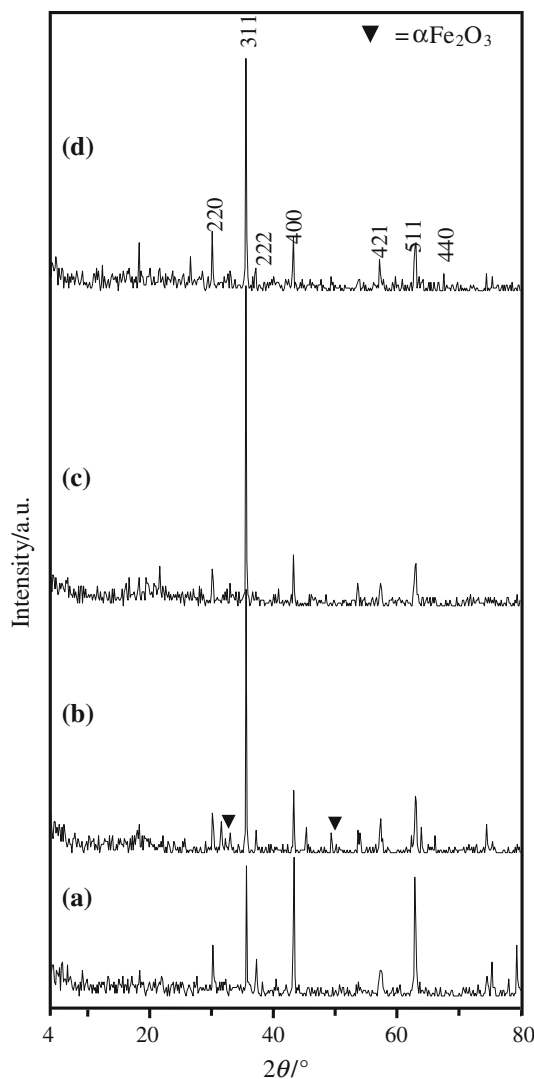
Fig. 2 XRD patterns of (*a*) PVA-free NiFe$_2$O$_4$, (*b*) 0.1PVA/NiFe$_2$O$_4$, (*c*) 0.2PVA/NiFe$_2$O$_4$, and (*d*) 0.3PVA/NiFe$_2$O$_4$

Raising the calcination temperature to 873 K results in the increase of the peak intensity at $d = 2.95$ Å characteristic of NiFe$_2$O$_4$ phase with a subsequent decrease in the peak intensity of free α-Fe$_2$O$_3$ phase at $d = 2.51$ Å. A further increase in temperature to 1,173 K simulates only the existence of the nickel ferrite phase through vanishing reflections of α-Fe$_2$O$_3$ phase. The average size of the NiFe$_2$O$_4$ crystals varied relatively from 47 nm at 673 K to 145 nm at 1,173 K.

The effect of PVA loadings on the crystalline phase composition of NiFe$_2$O$_4$ in comparison with PVA-free NiFe$_2$O$_4$ is shown in Fig. 2. The PVA-modified NiFe$_2$O$_4$ samples generally exhibit reflections of various planes indexed as (220), (311), (222), (400), (422), (511), and (440) owing to the presence of the cubic spinel structure. This result imparts a clear evidence for the NiFe$_2$O$_4$ formation according to the standard JCPDS (Card No. 10-325)

Table 1 The effects of addition of PVA to citric acid on the intensity values of *hkl* planes of $NiFe_2O_4$ phase

Samples	Crystal size/nm	Peak height/a.u.		
		I_{440}	I_{551}	I_{220}
PVA-free $NiFe_2O_4$	126.7	53	27	65
0.1PVA/$NiFe_2O_4$	169.1	27	37	23
0.2PVA/$NiFe_2O_4$	148.4	28	38	24
0.3PVA/$NiFe_2O_4$	147.8	33	34	27

[41]. Phase analysis of the 0.1PVA/$NiFe_2O_4$ pattern revealed the presence of α-Fe_2O_3 at *d* spacings 2.949, 2.698, and 2.203 Å, along with key lines of $NiFe_2O_4$. When the PVA concentration increased to 0.2–0.3 mol%, a single phase comprising merely of $NiFe_2O_4$ was depicted; emphasizing the beneficial effect of PVA in eliminating impurities that deteriorate the formation of a distinct phase $NiFe_2O_4$.

The most intense XRD peak at $2\theta = 36.16°$ and its respective plane at $d = 2.483$ Å corresponding to the (311) plane of $NiFe_2O_4$ are indicative of the presence of inverse spinel structure [42]. As reported earlier, the intensities of the (220), (440), and (511) planes are more sensitive to the cations in tetrahedral (A) and octahedral (B) coordinated sites, surrounded by oxygen atoms in the composite oxide [43, 44]. Fe^{3+} ions have tendency to occupy A sites, while Ni^{2+} ions appear to compete with Fe^{3+} ones to occupy B sites in the mixed ferrites. It is likely that the high concentrations of PVA significantly stabilize the Fe^{3+} ions in A sites in which the composition exhibit single-phase cubic spinel structure. Table 1 shows the observed intensities of the above three planes. The intensity of the (440) peak was observed to increase as the concentration of PVA increased; which infers the Ni^{2+} ions occupying the B site, i.e., the octahedral sites on the (440) plane. However, the intensity of the (220) plane increases by the continuous PVA addition indicating the preferential occupation of A sites by Fe^{3+} ions since $NiFe_2O_4$ is established to be an inverse spinel structure. Therefore, any distortion in the structure is caused by the migration of more number of Ni^{2+} ions to the tetrahedral site during sintering. The crystallite sizes of the synthesized powders are listed in Table 1 using the X-ray broadening of the (311) diffraction peak, via the well-known Scherrer's equation.

It must be noted that the citrate method may occur statistically at some regions of the nanoparticles causing a minor distortion. Thus, the steps taken for the formation of a single-phase ferrite by maintaining the citrate method are unsuccessful. Inversely, it seems that combining CA with PVA will stimulate the improved preparation of single-phase $NiFe_2O_4$. As the carbon chains in CA and PVA decompose during combustion, the adjacent atoms which
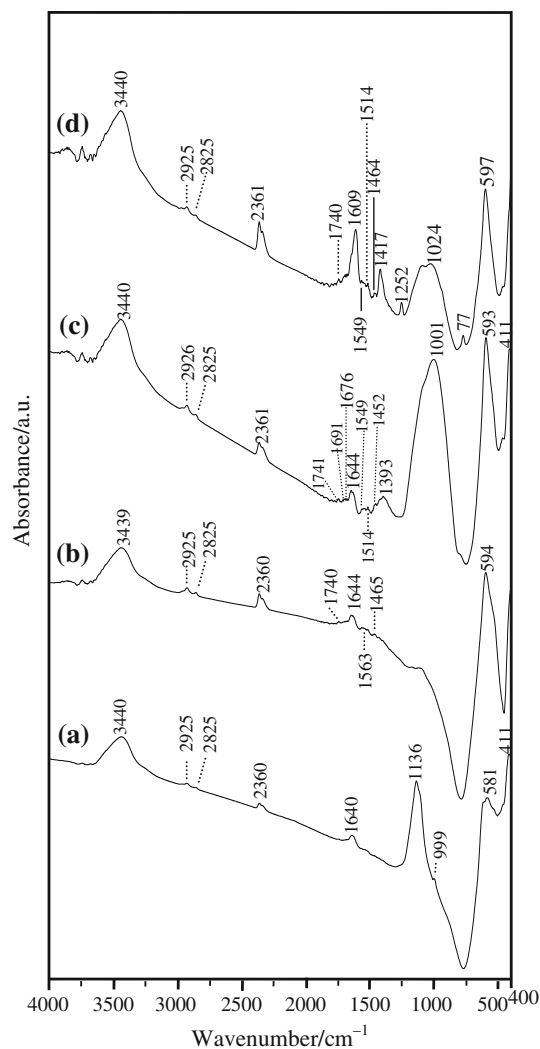
Fig. 3 FT-IR absorbance spectra of (*a*) PVA-free $NiFe_2O_4$, (*b*) 0.1PVA/$NiFe_2O_4$, (*c*) 0.2PVA/$NiFe_2O_4$, and (*d*) 0.3PVA/$NiFe_2O_4$

are homogeneously distributed throughout the matrix can easily come into contact and form crystal lattice at a considerable rate.

IR analysis

The synthesis of the ferrite spinel $NiFe_2O_4$ by treatment primarily with CA solution in the absence and presence of PVA polymeric intermediates was probed by FT-IR spectroscopy, as shown in Fig. 3. All the spectra characterized by two bands at 597 and 410 cm⁻¹, which are assigned to stretching vibration of overlap integrals between Fe^{3+} and O^{2-} ions, involve tetrahedral and octahedral coordinations in typical inverse spinel ferrites, respectively [19, 45]. The O–H stretching vibration associated with CA/PVA is observed at 3,440 cm⁻¹ for all the samples. However, the greater the concentration of the PVA, the more intense and broader the absorption of this band, which can be a result of

the superposition of multiple hydrogen bonds associated with the PVA crystalline phase [30]. The observed bands at 2918, 2852, and 1457 cm^{-1} are assigned to the anti-symmetric, symmetric, and bending of CH_2 vibrations, respectively, of the carbon chains in the PVA structure [46].

The ν_4 vibration doublet at approximately 1,644 and 1,609 cm^{-1} for the protonated complex $\equiv$Fe–O–COOH [47] was observed for 0.2PVA/NiFe$_2$O$_4$ and 0.3PVA/NiFe$_2$O$_4$ samples (Fig. 3c, d). It is noteworthy that this species grew largely as a function of PVA concentration, though the bands of this species were absent for PVA-free NiFe$_2$O$_4$ (Fig. 3a), which can verify the interaction between the Fe(III) ions and the CA/PVA matrix. This result was further confirmed by the presence of two bands at 1,549 and 1,401 cm^{-1} in the spectrum of the latter sample which are assigned to asymmetric and symmetric vibrations of the carboxylate –COO$^-$ groups, respectively. When compared with the frequencies of free carboxylate, these bands are shifted downward by small values to make firmer the presence of metal–carboxylate adducts through Fe(III) ions-chelating CA/PVA [48, 49]. The peak at 1,740 cm^{-1} for all samples prepared by adding PVA was assigned to the carbonyl stretch C=O group. The bands at 1,136 and 1,024 cm^{-1} in Fig. 3a, c, d are attributed to the organic network or COH groups [37]. These bands did not appear in the spectrum of 0.1PVA/NiFe$_2$O$_4$ sample, indicating the formation of pure NiFe$_2$O$_4$ compound at this concentration of incorporated PVA, i.e., 0.1 mol%. Meanwhile, the observed intense IR peaks of this organic species in the other samples indicate the incomplete combustion of the organic intermediates.

Thermal analysis

Thermal degradation of nickel ferrite–CA samples with respect to PVA concentration was studied by TG analysis (TG/DTG) (Fig. 4). The TG curve of PVA-free NiFe$_2$O$_4$ exhibits mass loss which occurs in two stages of temperatures in the range 303–1,273 K. The first mass loss (62.11 %) took place between 404 and 718 K due to the evaporation of absorbed water and decomposition of CA. The second stage indicates mass loss (2.33 %) at 1,022–1,268 K due to simultaneous condensation of the lattice oxygen and formulation of carbon metals/metal oxides. The addition of PVA (0.1–0.3 mol%) to form NiFe$_2$O$_4$ led to three mass loss stages in the temperature range 303–1,273 K. The first loss that occurred at 303–573 K is due to the decomposition of CA and evaporation of water molecules through dehydration reaction of PVA in the local segments of its molecular chain in which the main PVA could be turned into polyacetylene (–CH=CH–)$_n$. The second stage at 579–885 K showed increased mass losses comprising 28.275 % for 0.1PVA/ NiFe$_2$O$_4$, 21.996 % for 0.2PVA/NiFe$_2$O$_4$, and 52.835 %
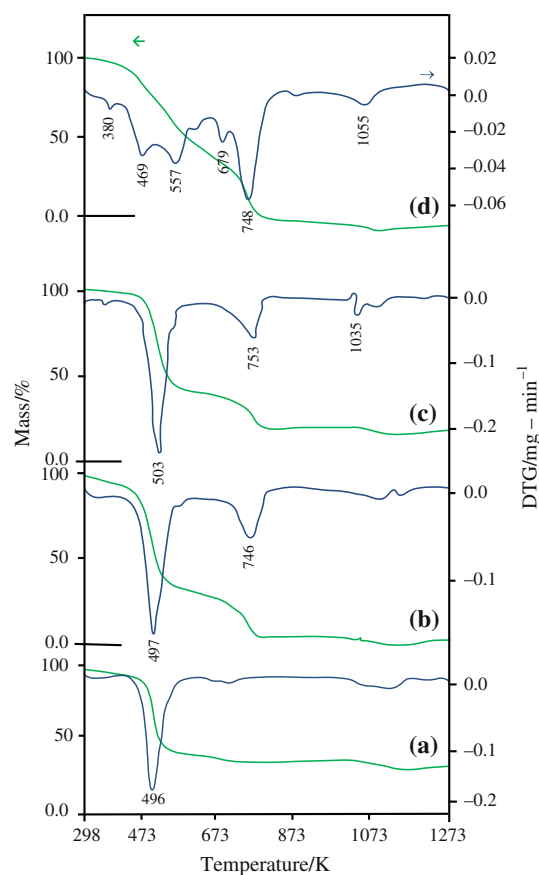
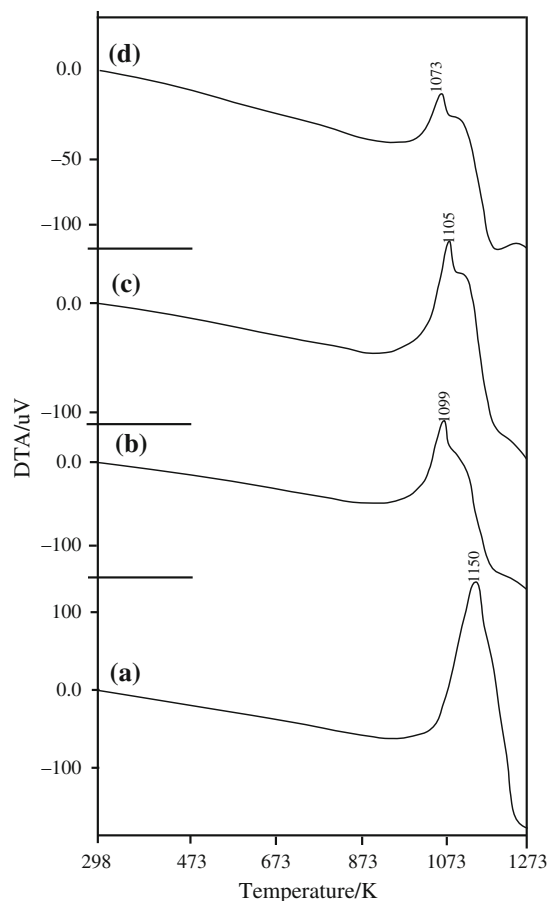**Fig. 4** TG and DTG profiles of (*a*) PVA-free NiFe$_2$O$_4$, (*b*) 0.1PVA/ NiFe$_2$O$_4$, (*c*) 0.2PVA/NiFe$_2$O$_4$, and (*d*) 0.3PVA/NiFe$_2$O$_4$

for 0.3PVA/NiFe$_2$O$_4$ due to mainly the elimination reactions that happened between residual acetate groups and partially can be products of hydrolyzed PVA. The third stage that experienced a mass loss of 2.958 % at 804–1,243 K in the profile of 0.3PVA/NiFe$_2$O$_4$ is indicative of further degradation process to yield hydrocarbons and metallic residues [50].

DTA curves (Fig. 5) obtained for PVA-free NiFe$_2$O$_4$, and 0.1PVA/, 0.2PVA/, and 0.3PVA/NiFe$_2$O$_4$ showed exothermic peaks at 1150, 1099, 1105, and 1073 K, respectively, which are attributed to different degradation processes [51]. Upon addition of PVA, a random change in glass-transition temperature can be achieved as compared with PVA-free NiFe$_2$O$_4$ that presented a greater decomposition temperature comparatively. This suggests that the segmental mobility of amorphous PVA becomes more rigid [52]. The concurrent lowering of decomposition temperature from 1,150 to 1,073 K upon increasing the PVA concentration may be due to reduction in molecular mass of PVA and/or breaking of inter- and intra-molecular PVA hydrogen bonding [53].

The kinetic parameters are listed in Table 2 and the following remarks can be pointed out: (i) the correlation
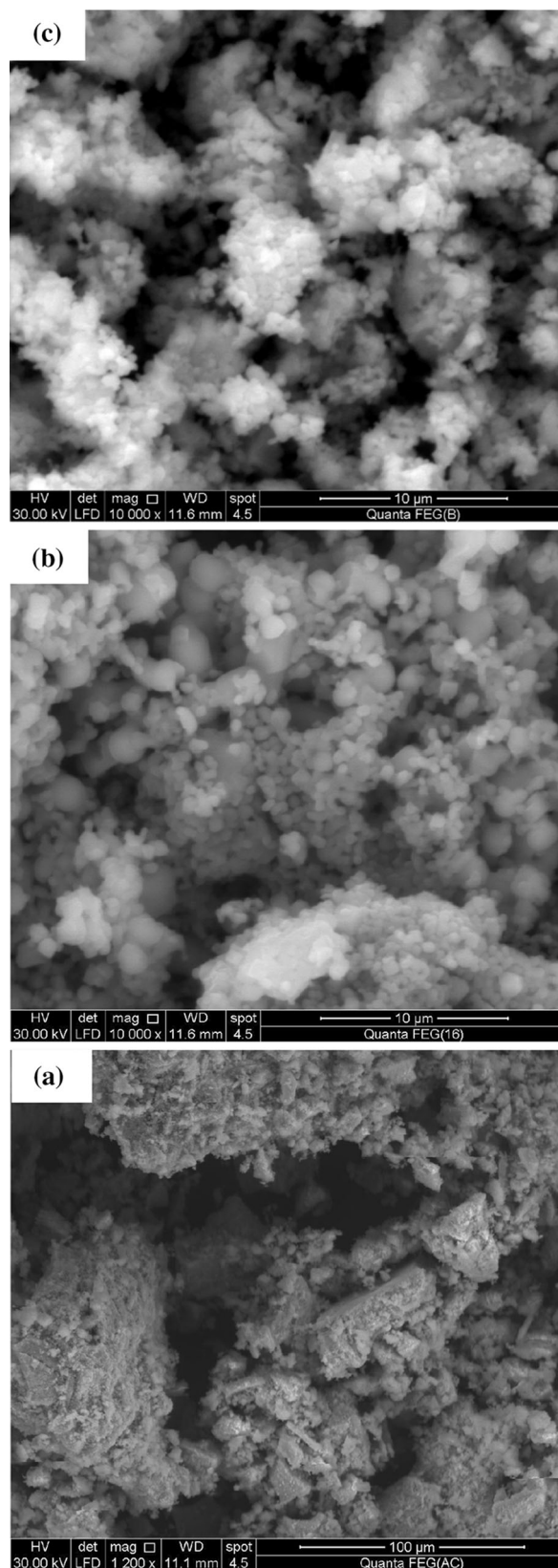
Fig. 5 DTA profiles of (*a*) PVA-free NiFe$_2$O$_4$, (*b*) 0.1PVA/NiFe$_2$O$_4$, (*c*) 0.2PVA/NiFe$_2$O$_4$, and (*d*) 0.3PVA/NiFe$_2$O$_4$

coefficient, r, which was computed using the least square method was higher than 0.99, indicating a good linearity for the experimental data; (ii) for most of samples, the negative ΔS^* values indicate an ordered activated intermediate in spite of tending to show a disorder behavior as the PVA concentration increases [54]. However, the trend that directs to the disorder by increasing the concentration of PVA may be caused in consequence of water loss. The positive values of ΔH^* mean that the decomposition processes are endothermic ones; (iii) as shown in Table 2, the E_a values at the regarded temperatures revealed that the water and anion molecules are easily eliminated by increasing the PVA amounts, as shown by the following sequence:

0.3PVA/NiFe$_2$O$_4$ > 0.2PVA/NiFe$_2$O$_4$ >

0.1PVA/NiFe$_2$O$_4$ > PVA free NiFe$_2$O$_4$.

The values of E_a for all the samples somewhat refer to a weak bonding between NiFe$_2$O$_4$ and PVA molecules. Besides, the E_a values of the first step are lower than the other steps as a result of its high rate of decomposition

Fig. 6 SEM micrographs of **a** PVA-free NiFe$_2$O$_4$, **b** 0.1PVA/NiFe$_2$O$_4$, and **c** 0.2PVA/NiFe$_2$O$_4$

Table 2 Decomposition temperature, order, and activation parameters of $NiFe_2O_4$ prepared by different concentrations of PVA

Samples	Steps	T/K	Log A/S^{-1}		E/kJ mol^{-1}		R^2
			CR	HM	CR	HM	CR
PVA-free $NiFe_2O_4$	First	496	1.35×10^4	3.62×10^5	50.96	57.98	0.9578
0.1PVA/$NiFe_2O_4$	First	497	4.51×10^5	1.60×10^6	48.50	63.86	0.9629
	Second	746	1.43×10^9	2.28×10^{10}	145.62	154.80	0.9483
0.2PVA/$NiFe_2O_4$	First	503	1.78×10^5	7.32×10^6	60.00	70.61	0.9871
	Second	753	2.10×10^{13}	4.83×10^{14}	202.24	216.42	0.9996
	Third	1,035	1.49×10^{16}	1.56×10^{18}	361.83	368.00	0.9220
0.3PVA/$NiFe_2O_4$	First	380	2.39×10^2	1.24×10^4	26.08	33.81	0.9928
	Second	469	5.76×10^2	1.39×10^4	33.52	42.88	0.9668
	Third	557	5.53×10^9	3.29×10^{11}	111.27	126.09	0.9733
	Fourth	679	5.56E+08	2.54E+10	127.24	140.87	0.9890
	Fifth	748	1.11×10^{15}	7.94×10^{15}	230.23	232.04	0.9605

Samples	R^2	ΔH^*/kJ mol^{-1}		ΔS^*/kJ mol^{-1} K^{-1}		ΔG^*/kJ mol^{-1}	
	HM	CR	HM	CR	HM	CR	HM
PVA-free $NiFe_2O_4$	0.9538	46.84	53.86	−0.170	−0.143	131.20	124.67
0.1PVA/$NiFe_2O_4$	0.9570	44.37	59.73	−0.141	−0.130	114.41	124.54
	0.9359	139.42	148.59	−0.077	−0.054	197.12	189.10
0.2PVA/$NiFe_2O_4$	0.9907	55.82	66.44	−0.149	−0.118	130.61	125.68
	0.9999	195.98	210.16	0.002	0.029	194.17	188.71
	0.9246	353.22	359.40	0.054	0.093	296.96	263.13
0.3PVA/$NiFe_2O_4$	0.9999	22.92	30.64	−0.202	−0.169	99.52	94.77
	0.9852	29.62	38.98	−0.196	−0.169	121.54	118.48
	0.9712	106.64	121.46	−0.064	−0.030	142.06	137.97
	0.9882	121.59	135.23	−0.084	−0.053	178.86	170.92
	0.9574	224.01	225.82	0.035	0.052	197.46	187.04

[55]; (iv) the values of the activation free energy ΔG^* which increase significantly for the subsequent decomposition stages for nickel ferrites indicate the non-spontaneous behavior. This is due to increasing the values of $T\Delta S^*$ significantly from one step to another and thus overriding the values of ΔH^*. Increasing the values of ΔG^* for the subsequent steps reflects increasing either CA or PVA removal rate which will be lower than that of the precedent citrate with PVA. This may be attributed to the structural rigidity of the remaining nickel ferrite after the expulsion of one species and/or more (citrate or PVA), as compared with the precedent sample, which requires more energy, $T\Delta S^*$, for its rearrangement before undergoing any compositional change; and (v) there is an apparent gap in the values of the heat of activation E^* and the enthalpy of activation ΔH^* of volatilized of species between 0.3PVA/$NiFe_2O_4$ ($\Delta H^* = 29.62$ kJ mol^{-1}) and PVA-free sample ($\Delta H^* = 46.84$ kJ mol^{-1}). This may be attributed to the packing structure of $NiFe_2O_4$ which may allow stronger interactions of CA molecules in the crystal.

Scanning electron microscopy (SEM)

SEM analysis was performed in order to depict the microstructure of the synthesized $NiFe_2O_4$ through treatment primarily with CA solution, in the absence and presence of different loadings of PVA polymeric intermediate; and calcination at 1,173 K (Fig. 6). For PVA-free $NiFe_2O_4$, the SEM micrographs exhibited foamy-like agglomerated particles with a wide distribution, along with the presence of large voids in the matrix (Fig. 6a). On the other hand, the image of 0.1PVA/$NiFe_2O_4$ was characterized by the presence of both large and small spherical particles that are distributed in a homogeneous manner in this sample (Fig. 6b). The former particles may correlate to α-Fe_2O_3, compatible with XRD. However, this image looks different from that of the main structure of ferrites. When PVA loading increased (i.e., 0.2PVA/$NiFe_2O_4$), the spheriform shape of the particles as well as slight agglomeration of the very fine particles emerged due to intrinsic nickel ferrite. This result strongly supports that the addition of PVA plays
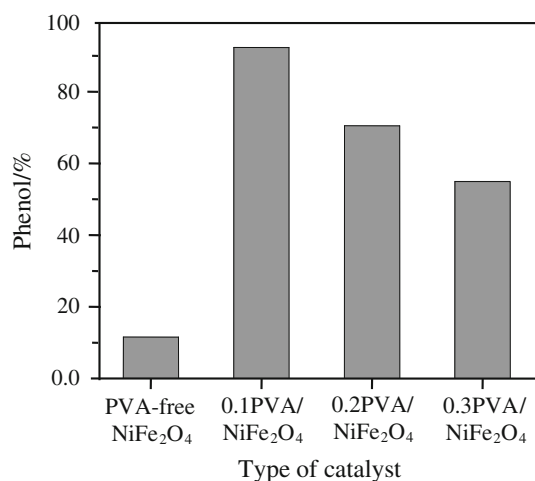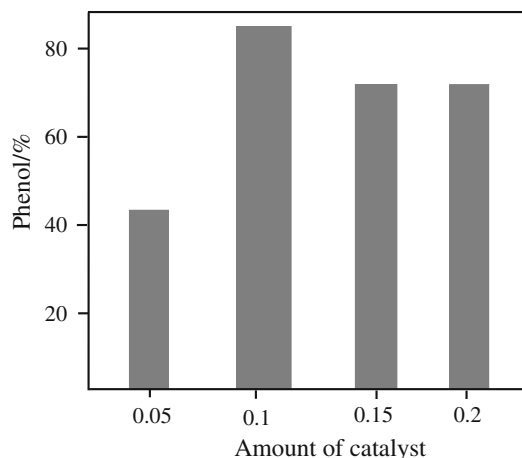
Fig. 7 Hydroxylation of benzene as a function of type of catalyst; reaction conditions: pressure 1 atm, temperature 353 K, catalyst amount 0.10 g, concentration of H$_2$O$_2$ 0.011 mol, concentration of benzene 0.022 mol, and reaction time 1 h

Fig. 8 Hydroxylation of benzene to phenol using different amounts of 0.1PVA/NiFe$_2$O$_4$ catalyst, reaction conditions: pressure 1 atm, temperature 353 K, catalyst amount 0.010, 0.015, 0.10, and 0.20 g, concentration of H$_2$O$_2$ 0.011 mol, concentration of benzene 0.022 mol, and reaction time 1 h

a structure-directing agent which improves the nucleation. The enhanced nucleation has thus led to the formation of smaller particle size.

Formation mechanism of NiFe$_2$O$_4$

Both types of chelating agents, namely PVA (hydroxyl chelating agent) and CA (carboxyl chelating agent) were used to coordinate Ni(II) and Fe(III) to form either a mono- or bi-dendate metal complexes [56], in which undesired spontaneous condensation reactions would be prohibited [57]. This can be visually verified through color changes observed when ferric and nickel precursors are added to water encompassing PVA with CA at ambient conditions. In the absence of PVA with CA, ferric chloride is oxidized by oxygen-enriched air and the solution turned turbid after a short period of time. However, no color change is observed when ferric chloride is added to the PVA solution, indicating that Fe^{3+} cations are sterically entrapped in the entangled network of the organic polymer [58].

The use of chelating agents was essential for the production of more nickel ferrite phases in the final product. Two possible mechanisms can explain this observation. The first mechanism is associated with the molecular structure of the hybrid organic–inorganic complex of both nickel and iron ions, since the chelating agent might prevent any initial condensation or any cross-linking between PVA and CA [59] during the preparation stage. The strongly charged ferric ions are neutralized by the PVA and CA anions, and would diffuse into their integrity until they become uniformly surrounded by the less charged nickel ions. This process of diffusion ensured that the energy of the system would approach a minimum value.

The second mechanism involved an enhanced T_g of the solution while oxidizing PVA during heat treatment. The melting enthalpy (ΔH) decreased (from 1,150 to 1,073 K) as the PVA concentration increased, suggesting reduction in intermolecular forces in the presence of CA-crosslinked PVA networks. According to phase investigation of 0.2PVA by XRD and SEM, we found that this sample exhibited majority of the nickel ferrite phase. Plausibly, the chelating agents influence the reaction temperature of phase formation. It may also enhance the dynamics of the oxidation reaction from the ground state to the optimum condition to form molten nickel ferrite phase. Note that the PVA concentration must be sufficient to obtain a uniform distribution of cations, and hence isolate the particles by a polymer layer [60], as shown by SEM analysis (Fig. 6). The weak hydrogen bonding in the hydrated PVA also plays a role in promoting homogeneous physical entrapment between the hydroxyl groups and cations, which are solvated by water molecules [58], thereby hindering aggregation and resulting in a relatively uniform particle size distribution. Moreover, the chelate effect of mutual hydroxyl and carboxyl chelating agents of CA–PVA appears more effective than carboxyl chelating agent of CA merely in producing more completely molten splats and nickel ferrite phase.

Catalytic activity

Composite catalysts of NiFe$_2$O$_4$ prepared by adding varying amounts of PVA (0.1–0.3 mol%) have been used for the one-step direct hydroxylation of benzene toward phenol in the presence of hydrogen peroxide (30 % aq.) as a green oxidant at 353 K as water is the only by-product (Eq. (9)). The phenol concentrations produced from the hydroxylation reaction have been plotted against time (Fig. 7). The
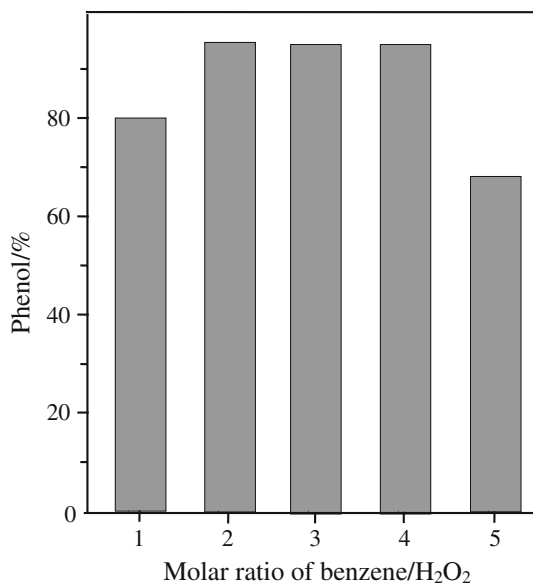
Fig. 9 Conversion of benzene to phenol over 0.1PVA/NiFe$_2$O$_4$ as a function of molar ratio of benzene:H$_2$O$_2$, reaction conditions: pressure 1 atm, temperature 353 K, catalyst amount 0.1 g, concentration of H$_2$O$_2$ 0.011 mol, concentration of benzene 0.011, 0.022, 0.033, 0.044 and 0.055 mol, 20 mL water, and reaction time 1 h
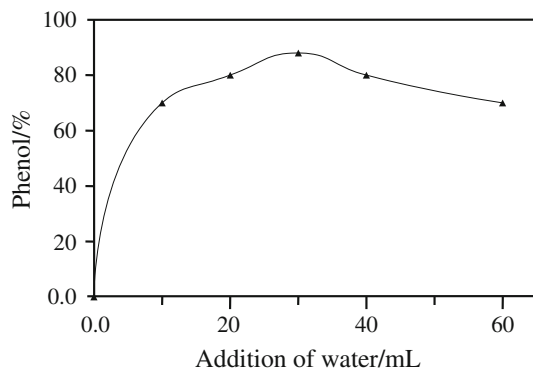
Fig. 10 Conversion of benzene to phenol as a function of added water over 0.1PVA/NiFe$_2$O$_4$, reaction conditions: pressure 1 atm, temperature 353 K, catalyst amount 0.1 g, concentration of H$_2$O$_2$ 0.011 mol, concentration of benzene 0.022 mol, and reaction time 1 h

0.1PVA/NiFe$_2$O$_4$ catalyst exhibited higher activity in benzene hydroxylation compared to other catalysts [18, 61, 62].

$$(9)$$
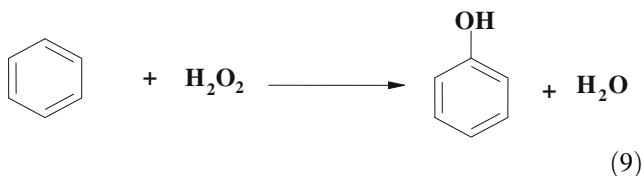
Influence of catalyst amount

Figure 8 shows the relationship between conversion of substrate and the amount of 0.1PVA/NiFe$_2$O$_4$ catalyst in

the hydroxylation of 50 mL pure benzene. It indicates that the catalytic activity increases to produce a higher yield of phenol (95 %) with increasing amount of catalyst till 0.1 g. Hence, the reaction rate of this reaction is dependent on the catalyst amount [63, 64].

Effect of molar ratio of benzene/H$_2$O$_2$

As illustrated in Fig. 9, benzene conversion on 0.1 g of 0.1PVA/NiFe$_2$O$_4$ was found to increase with increasing benzene/H$_2$O$_2$ molar ratio up to 2:1, reaching 96 % conversion and level-off at this ratio even though the molar ratio was further increased to 4:1.

Effect of added water to the reaction mixture

Figure 10 illustrates the effect of adding water to the reaction mixture composed of benzene/H$_2$O$_2$ and 0.1 g of 0.1PVA/NiFe$_2$O$_4$ on benzene conversion into phenol. Increasing the volume of added water to 30 mL causes a significant increase in the conversion percentage. However, blank experiments in the absence of H$_2$O$_2$ indicated that no direct reaction occurred under these conditions between either benzene and water or phenol and water. Increasing water volume to 40 mL decreases the conversion. This can be explained in the sense that water helps to strip phenol away from the catalytically active sites, thereby preventing further oxidation of phenol.

Conclusions

PVA was found to be an effective surfactant for the hydrothermal synthesis of NiFe$_2$O$_4$ at a molar ratio of Fe:Ni = 2.63 (w/w) in the presence of consistent concentration of CA. Distinctive preparations refer to the conditions of the calcination and period of aging. While calcination at 1,173 K exhibits only a single phase of NiFe$_2$O$_4$, lowering the temperature to 673–873 K presumed the formation of Fe$_2$O$_3$ and NiFe$_2$O$_4$ phases. As the period of aging was increased at 1,173 K, an enhancement generally occurred in crystallinity as revealed from the XRD analysis. The kinetic parameters established on both CR and HM "model free" methods indicated considerable variation of the kinetic parameters E^* and A based on the diverse concentration of PVA-doped NiFe$_2$O$_4$. From these kinetic parameters, the elimination of water and organic CA/PVA species from nickel ferrites at the first temperature loss stage was facilitated according to the following order: 0.3PVA/NiFe$_2$O$_4$ > 0.2PVA/NiFe$_2$O$_4$ > 0.1PVA/NiFe$_2$O$_4$ > PVA-free NiFe$_2$O$_4$. The E^* values for the first stage is lower than the analogous stages as a result of high decomposition rate of CA/PVA. The lower ΔH^* value for

0.3PVA/NiFe$_2$O$_4$ (29.62 kJ mol^{-1}) than that for PVA-free NiFe$_2$O$_4$ (46.84 kJ mol^{-1}) may be attributed to the packing structure of NiFe$_2$O$_4$ which may allow stronger interaction of CA molecules with the PVA-free sample. The one-step direct hydroxylation of benzene with H$_2$O$_2$ has been extensively studied over the various preparations and demonstrated a range of catalytic activities following the order: 0.1PVA/NiFe$_2$O$_4$ > 0.2PVA/NiFe$_2$O$_4$ > 0.3PVA/NiFe$_2$O$_4$ > PVA-free NiFe$_2$O$_4$.

References

1. Gunjakar JL, More AM, Gurav KV, Lokhande CD. Chemical synthesis of spinel nickel ferrite (NiFe$_2$O$_4$) nano-sheets. Appl Surf Sci. 2008;254:5844–8.
2. Gopal Reddy CV, Manorama SV, Rao VJ. Preparation and characterization of ferrites as gas sensor materials. J Mater Sci Lett. 2000;19:775–8.
3. Nuli YN, Qin QZ. Nanocrystalline transition metal ferrite thin films prepared by an electrochemical route for Li-ion batteries. J Power Sources. 2005;142:292–7.
4. Gibson MA, Hightower JW. Oxidative dehydrogenation of butenes over magnesium ferrite kinetic and mechanistic studies. J Catal. 1976;41:420–30.
5. Manova E, Tsoncheva T, Paneva D, Mitov I, Tenchev K, Petrov L. Mechanochemically synthesized nano-dimensional iron–cobalt spinel oxides as catalysts for methanol decomposition. Appl Catal A. 2004;277:119–27.
6. Oliveira LCA, Fabris JD, Rios RRVA, Mussel WN. Fe$_{3-x}$Mn$_x$O$_4$ catalysts: phase transformations and carbon monoxide oxidation. Appl Catal A. 2004;259:253–9.
7. PalDey S, Gedevanishvii S, Zhang W, Rasouli F. Evaluation of a spinel based pigment system as a CO oxidation catalyst. Appl Catal B. 2005;56:241–50.
8. Xiong CR, Chen QL, Lu WR, Gao HX, Lu WK, Gao Z. Novel Fe-based complex oxide catalysts for hydroxylation of phenol. Catal Lett. 2000;69:231–6.
9. Sreekumar K, Sugunan S. Ferrospinels based on Co and Ni prepared via a low temperature route as efficient catalysts for the selective synthesis of o-cresol and 2,6-xylenol from phenol and methanol. J Mol Catal A. 2002;185:259–68.
10. Kinemuchi Y, Ishizaka K, Suematsu H, Jiang W, Yatsui K. Magnetic properties of nanosize NiFe$_2$O$_4$ particles synthesized by pulsed wire discharge. Thin Solid Films. 2002;407:109–13.
11. Kale A, Gubbala S, Misra RDK. Magnetic behavior of nanocrystalline nickel ferrite synthesized by the reverse micelle technique. J Magn Magn Mater. 2004;277:350–8.
12. Urda A, Herraiz A, Redey A, Marcu IC. Co and Ni ferrospinels as catalysts for propane total oxidation. Catal Commun. 2009;10:1651–5.
13. Florea M, Alifanti M, Parvulescu VI, Mihaila-Tarabasanu D, Diamandescu L, Feder M, Negrila C, Frunza L. Total oxidation of toluene on ferrite-type catalysts. Catal Today. 2009;141:361–6.
14. Xu S, Shangguan W, Yuan J, Chen M, Shi J. Preparations and photocatalytic properties of magnetically separable nitrogen-doped TiO$_2$ supported on nickel ferrite. Appl Catal B. 2007;71:177–84.
15. Russo N, Fino D, Saracco G, Specchia V. N$_2$O catalytic decomposition over various spinel-type oxides. Catal Today. 2007;119:228–32.
16. Lee H, Jung JC, Kim H, Chung Y-M, Kim TJ, Lee SJ, Oh S-H, Kim YS, Song IK. Effect of divalent metal component (Me^{II}) on the catalytic performance of Me^{II}Fe$_2$O$_4$ catalysts in the oxidative dehydrogenation of n-butene to 1,3-butadiene. Catal Lett. 2008;124:364–8.
17. Feng S, Yang W, Wang Z. Synthesis of porous NiFe$_2$O$_4$ microparticles and its catalytic properties for methane combustion. Mater Sci Eng B. 2011;176:1509–12.
18. Ren Y, Dong Q, Feng J, Ma J, Wen Q, Zhang M. Magnetic porous ferrospinel NiFe$_2$O$_4$: a novel ozonation catalyst with strong catalytic property for degradation of di-n-butyl phthalate and convenient separation from water. J Colloid Interface Sci. 2012;382:90–6.
19. Gotic M, Czako-Nagy I, Popovic S, Music S. Formation of nanocrystalline NiFe$_2$O$_4$. Philos Mag Lett. 1998;78:193–201.
20. Schaefer H, Kisker H, Kronmuller H, Wurschum R. Magnetic properties of nanocrystalline nickel. Nanostruct Mater. 1992;1:523–9.
21. Nathani H, Gubbala S, Misra RDK. Magnetic behavior of nanocrystalline nickel ferrite. Part I. The effect of surface roughness. Mater Sci Eng B. 2005;121:126–36.
22. El-Shobaky GA, Fagal GA, Abd el-Aal A, Ghozza AM. Solid–solid interactions in the NiOFe$_2$O$_3$ system with and without LiO$_2$ doping. Thermochim Acta. 1995;256:429–41.
23. Xiao SH, Jiang WF, Li LY, Li XJ. Low-temperature auto-combustion synthesis and magnetic properties of cobalt ferrite nanopowder. Mater Chem Phys. 2007;106:82–7.
24. Habibi MH, Habibi AH, Zendehdel M, Habibi M. Dye-sensitized solar cell characteristics of nanocomposite zinc ferrite working electrode: effect of composite precursors and titania as a blocking layer on photovoltaic performance. Spectrochim Acta A. 2013;110:226–32.
25. Habibi M, Habibi A. Effect of the thermal treatment conditions on the formation of zinc ferrite nanocomposite, ZnFe$_2$O$_4$, by sol–gel method. J Therm Anal Calorim. 2013;113:843–7.
26. Hyeon T. Chemical synthesis of magnetic nanoparticles. Chem Commun. 2003;8:927–34.
27. Stober W, Fink A, Bohn EJ. Controlled growth of monodisperse silica spheres in the micron size range. J Colloid Interface Sci. 1968;26:62–9.
28. Kommareddi NS, Tata M, Jhon VT, McPherson GL, Herman MF, Lee YS. Synthesis of superparamagnetic polymer–ferrite composites using surfactant microstructures. Chem Mater. 1996;8:801–9.
29. Lelis MFF, Porto AO, Goncalves CM, Fabris JD. Cation occupancy sites in synthetic Co-doped magnetites as determined with X-ray absorption (XAS) and Mössbauer spectroscopies. J Magn Magn Mater. 2004;278:263–9.
30. Kamellia N, Zabihi R. Preparation and magnetic properties of nano size nickel ferrite particles using hydrothermal method. Chem Cent J. 2012;6:23. doi:10.1186/1752-153X-6-23.
31. Hasab GM, Seyyed Ebrahimi SA, Badiei A. An investigation on physical properties of strontium hexaferrite nanopowder synthesized by a sol–gel auto-combustion process with addition of cationic surfactant. J Eur Ceram Soc. 2007;27:3637–40.
32. Bragg WH, Bragg WL. The structure of the diamond. Nature. 1913;91:557–558.
33. Kissinger HE. Variation of peak temperature with heating rate in differential thermal analysis. J Res Natl Bureau Stand. 1956;57:217–21.
34. Burnham AK, Braun RL. Global kinetic analysis of complex materials. Energy Fuels. 1999;13:1–22.
35. Coats AW, Redfern JP. Kinetic parameters from thermogravimetric data. Nature. 1964;201:68–9.
36. Horowitz HH, Metzger G. A new analysis of thermogravimetric traces. Anal Chem. 1963;35:1464–8.

37. Nath M, Arora P. Spectral and thermal studies of cobalt(II), nickel(II) and copper(II) complexes of schiff bases obtained from *o*-hydroxyacetophenone and amino acids. Synth React Inorg Met Org Chem. 1993;23:1523–46.

38. Soliman AA, El-Medani SM, Ali OAM. Thermal study of chromium and molybdenum complexes with some nitrogen and nitrogen–oxygen donors ligands. J Therm Anal Calorim. 2006; 83:385–92.

39. Greenberg AE, Clesceri LS, Eaton AD, editors. Standard methods for the examination of water and wastewater. 17th ed. Washington, DC: American Public Health Association (APHA); 1989.

40. Tor A, Cengeloglu Y, Aydin ME, Ersoz M. Removal of phenol from aqueous phase by using neutralized red mud. J Colloid Interface Sci. 2006;300:498–503.

41. Fu YP, Pan KY, Lin CH. Ni–Cu–Zn ferrite powder from steel pickled liquor and electroplating waste solutions. Mater Lett. 2002;57:291–6.

42. Maensiri S, Masingboon C, Boonchom B, Seraphin S. A simple route to synthesize nickel ferrite ($NiFe_2O_4$) nanoparticles using egg white. Scr Mater. 2007;56:797–800.

43. Ladgaonkar BP, Vaingainkar AS. X-ray diffraction investigation of cation distribution in $Cd_\chi Cu_{1-\chi}Fe_2O_4$ ferrite system. Mater Chem Phys. 1998;56:280–3.

44. John Berchmans L, Kalai Selvan R, Selva Kumar PN, Augustin CO. Structural and electrical properties of $Ni_{1-x}Mg_xFe_2O_4$ synthesized by citrate gel process. J Magn Magn Mater. 2004;279: 103–10.

45. Gunjakar JL, More AM, Shinde VR, Lokhande CD. Synthesis of nanocrystalline nickel ferrite ($NiFe_2O_4$) thin films using low temperature modified chemical method. J Alloy Compd. 2008;465:468–73.

46. Socrates G. Infrared and Raman characteristic group frequencies: tables and charts. 3rd ed. Chichester: Wiley; 2001.

47. Su C, Suarez DL. In situ infrared speciation of adsorbed carbonate on aluminum and iron oxide. Clay Clay Miner. 1997;45:814–25.

48. Zeng X, Liu Y, Wang X, Yin W, Wang L, Guo H. Preparation of nanocrystalline $PbTiO_3$ by accelerated sol–gel process. Mater Chem Phys. 2002;77:209–14.

49. Rama Rao GV, Surya Narayana DS, Varadaraju UV, Rao GVN, Venkadesan S. Synthesis of $YBa_2Cu_3O_7$ through different gel routes. J Alloys Compd. 1995;217:200–8.

50. Peng Z, Kong LX. A thermal degradation mechanism of polyvinyl alcohol/silica nanocomposites. Polym Degrad Stab. 2007;92:1061–71.

51. Budrugeac P. Kinetics of the complex process of thermo-oxidative degradation of poly(vinyl alcohol). J Therm Anal Calorim. 2008;92:291–6.

52. Rajendran S, Sivakumar M, Subadevi R, Nirmale M. Characterization of PVA–PVdF based solid polymer blend electrolytes. Physica B. 2004;348:73–8.

53. Anbarasan R, Pandiarajaguru R, Prabhu R, Dhanalakshmi V, Jayalakshmi A, Dhanalakshmi B, Nisha SU, Gandhi S, Jayalakshmi T. Synthesis, characterizations, and mechanical properties of structurally modified poly(vinyl alcohol). J Appl Polym Sci. 2010;117:2059–68.

54. Frost AA, Pearson RG. Kinetics and mechanism. 2nd ed. New York: Wiley; 1961. p. 88–100.

55. West DX, Yang Y, Klein TL, Goldberg KI, Liberta AE, Valdes-Matinez J, Hernandez-Ortega S. Binuclear copper(II) complexes of 2-hydroxyaceto-phenone [4]*N*-substituted thiosemicarbazones. Polyhedron. 1995;14:1681–93.

56. Varma PCR, Colreavy J, Cassidy J, Oubaha M, Duffy B, McDonagh C. Effect of organic chelates on the performance of hybrid sol–gel coated AA 2024-T3 aluminium alloys. Prog Org Coat. 2009;66:406–11.

57. Oubaha M, Etienne P, Calas S, Coudray P, Nedelec J, Moreau Y. Sol–gel derived organic and inorganic hybrid materials for photonic applications: contribution to the correlation between the material structure and the transmission in the near infrared region. J Sol–Gel Sci Technol. 2005;33:241–8.

58. Lee SJ, Lee CH, Kriven WM. Synthesis of oxide ceramic powders by polymerized organic inorganic complex route. J Ceram Process Res. 2000;1:92–5.

59. Shi R, Bi J, Zhang Z, Zhu A, Chen A, Zhou X, Zhang L, Tian W. The effect of citric acid on the structural properties and cytotoxicity of the polyvinyl alcohol/starch films when molding at high temperature. Carbohydr Polym. 2008;74:763–70.

60. Lu J, Liu B, Yang H, Luo W, Zou G. Surface modification of $CrSi_2$ nanocrystals with polymer coating. Mater Sci Lett. 1998;17:1605–7.

61. Peng T, Zhang X, Lv H, Zan L. Preparation of $NiFe_2O_4$ nanoparticles and its visible-light-driven photoactivity for hydrogen production. Catal Commun. 2012;28:116–9.

62. Khosravi I, Eftekhar M. Characterization and evaluation catalytic efficiency of $NiFe_2O_4$ nano spinel in removal of reactive dye from aqueous solution. Powder Technol. 2013;250:147–53.

63. Othman I, Mohamed RM, Ibrahim IA, Mohamed MM. Synthesis and modification of ZSM-5 with manganese and lanthanum and their effects on decolorization of indigo carmine dye. Appl Catal A. 2006;299:95–102.

64. Canali L, Sherrington DC. Utilisation of homogeneous and supported chiral metal (salen) complexes in asymmetric catalysis. Chem Soc Rev. 1999;28:85–93.